

**OPEN ACCESS**

## Transport Properties in Electrodes for Lithium-Ion Batteries: Comparison of Compact versus Porous NCM Particles

To cite this article: Luca Schneider *et al* 2022 *J. Electrochem. Soc.* **169** 100553

View the [article online](#) for updates and enhancements.



The Electrochemical Society  
Advancing solid state & electrochemical science & technology

243rd ECS Meeting with SOFC-XVIII

**More than 50 symposia are available!**

Present your research and accelerate science

Boston, MA • May 28 – June 2, 2023

[Learn more and submit!](#)



# Transport Properties in Electrodes for Lithium-Ion Batteries: Comparison of Compact versus Porous NCM Particles

Luca Schneider,<sup>1</sup>  Julian Klemens,<sup>2</sup> Eike Christian Herbst,<sup>2</sup> Marcus Müller,<sup>1</sup> Philip Scharfer,<sup>2</sup> Wilhelm Schabel,<sup>2</sup> Werner Bauer,<sup>1,z</sup>  and Helmut Ehrenberg<sup>1</sup>

<sup>1</sup>Institute for Applied Materials (IAM), Karlsruhe Institute of Technology (KIT), 76344 Eggenstein-Leopoldshafen, Germany

<sup>2</sup>Thin Film Technology (TFT), Karlsruhe Institute of Technology (KIT), 76131 Karlsruhe, Germany

Previous investigations on porous  $\text{Li}(\text{Ni}_x\text{Co}_y\text{Mn}_z)\text{O}_2$  (NCM) particles with shortened diffusion paths and an enlarged interface between active material and electrolyte show improved rate capability and cycle stability compared to compact particles. Due to the additional intragranular porosity of the active material, also the pore structure of the overall electrode, and as consequence, the ionic transport in the pore phase is altered. In addition, the particle morphology influences the ohmic contact resistance between the current collector and electrode film. These effects are investigated using impedance spectroscopy in symmetrical cells under blocking conditions. The ionic resistance and the tortuosity of the electrodes are determined and analyzed by a transmission line model. Tortuosity is higher for porous particles and increases more during calendaring. This limits the options to densify these electrodes to the same level as with compact particles. In a further approach, the method is used to explain the drying related performance differences of these electrodes. At higher drying rates, the contact and the ionic resistance of electrodes with compact particles increases more strongly as for electrodes with porous particles. These investigations provide new insights into the ion transport behavior and enable a better understanding of the impact of the electrode processing condition.

© 2022 The Author(s). Published on behalf of The Electrochemical Society by IOP Publishing Limited. This is an open access article distributed under the terms of the Creative Commons Attribution 4.0 License (CC BY, <http://creativecommons.org/licenses/by/4.0/>), which permits unrestricted reuse of the work in any medium, provided the original work is properly cited. [DOI: 10.1149/1945-7111/ac9c37]



Manuscript submitted August 5, 2022; revised manuscript received October 13, 2022. Published October 31, 2022.

The most common used cathodes in lithium-ion batteries (LIB) are layered oxides, like  $\text{Li}(\text{Ni}_x\text{Co}_y\text{Mn}_z)\text{O}_2$  (NCM).<sup>1–3</sup> However, battery performance not only depends on the chemical composition of the active materials but also on the morphology, the structure of the particles, and electrodes. In particular, micro- and nanostructuring of active particles is a very effective approach to improve cell performance. The diffusion length within the active material is shortened, and to a special degree the diffusion time, which is proportional to the square of the length.<sup>4</sup> Furthermore, in the solid phase the diffusion coefficient is very low (e.g.  $10^{-10}$ – $10^{-11}$   $\text{cm}^2 \text{s}^{-1}$  for NCM)<sup>5</sup> compared to the diffusion coefficient in the electrolyte phase (e.g.  $10^{-6}$   $\text{cm}^2 \text{s}^{-1}$  for 1 M  $\text{LiPF}_6$  in EC:DMC, 1:1 (LP30)).<sup>6,7</sup> Beside lowering the diffusion length of the active material, a particle size reduction increases the specific surface of the powder. The rate performance is improved by increasing the contact area between the electrolyte and the active material, since the charge transfer takes place at the surface of the active material. To improve the performance and lifetime of the cells, a variety of adapted structures and shapes are described in the literature, such as preferentially oriented crystals within the particles,<sup>8</sup> nanobrick morphology,<sup>9</sup> one-dimensional hierarchical microrods,<sup>10</sup> and hierarchically structured particles.<sup>10–13</sup>

The synthesis of hierarchically structured particles is demonstrated in a two-step process consisting of agglomeration and partial sintering of nanoscale primary particles into micron-sized secondary particles with an open pore structure.<sup>13</sup> These particles have a higher C-rate performance compared to compact particles of the same size. During cycling, electrodes consisting of porous particles also exhibit lower probability of cracking.<sup>14</sup> Chen et al. explained that for smaller primary particles, a lower Li concentration gradient leads to lower mechanical stress.<sup>14</sup> In long time cycling tests, porous particles therefore exhibit higher state of health (SOH) than compact particles.<sup>15,16</sup>

For the evaluation of the impact of particle morphology on cell performance, it is necessary to consider not only the active material, but the entire electrode structure. An electrode consists of a solid phase containing active material, conductive additives and binder, while the liquid phase consists of an electrolyte that penetrates into the pores. The resistances of each phase influence the cycle

behavior: The contact resistance  $R_{\text{cont}}$  between the current collector and the electrode film, the electrical resistance  $R_{\text{el}}$  of the electrode particle system and the ionic resistance  $R_{\text{ion}}$  in the pore structure of the electrode. Various methods are used to investigate the individual resistance contributions. For example, tomography measurements can determine the distribution of the solid phase of the electrode and transfer it to a spatial model. Such measurements and statistical image analysis of the phases were performed by Neumann et al.<sup>17</sup> at NCM111 electrodes with compact and porous particles. Other approaches are of electrochemical nature such as rate capability tests (constant current), cyclic voltammetry (potential scan rate) and electrochemical impedance spectroscopy (EIS). While in rate stability tests and cyclic voltammetry, the overlapping of different parameters and effects determines the results, with EIS it is possible to separate processes and assign them to individual components.

In this work, EIS is used to investigate the influence of compact or porous particles (Fig. 1) on contact resistance  $R_{\text{cont}}$  and ionic resistance  $R_{\text{ion}}$  of NCM111 cathodes. The measurement setup is a symmetric cell under blocking conditions, which can distinguish reactions such as ion transport through pores and double layer formation of the effective surface by its frequency response.<sup>18</sup> In particular, the pore network of the electrodes with porous particles and the influence of drying and calendaring is investigated, since it is known from previous studies that porous particles can lead to improved electrode properties such as higher rate capability and less dependency on the drying rate for the investigated slurry configuration.<sup>15,16,19,20</sup> On the other hand, electrodes consisting of porous particles have higher porosity and, thus, lower energy density than those with compact particles. They therefore require high compaction and efficient drying conditions to reduce the porosity to levels known from compact particles. Since these measures affect the pore structure, EIS can be used to investigate the impact on the electrical arrangement and on the ion transport behavior of the electrodes.

## Theory

**Electrode tortuosity.**—The morphology of the pore system in battery electrodes has a strong influence on the transport behavior. The transport paths of the ions through the porous electrode are not straight, but they have to circumvent the active material, the binder and the conductive additives. The length of transport paths through

<sup>z</sup>E-mail: [werner.bauer@kit.edu](mailto:werner.bauer@kit.edu)

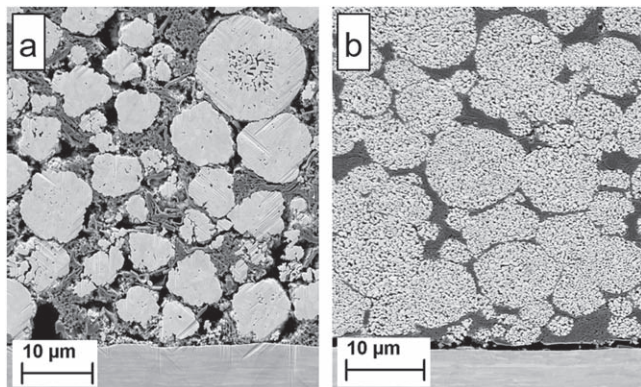


**Figure 1.** SEM micrographs of cross sections of calendared electrodes with (a) compact and (b) porous NCM particles. Porosity is 0.4 for both electrodes.

the pore system in relation to an ideal, straight-line path is described by the tortuosity. Here, it should be noted that there are many different notations for tortuosity in the literature.<sup>21–24</sup> One concept is the geodesic tortuosity  $\tau_{geo}$ , which is defined by the ratio between the average geometric pathway  $d_{path}$  following the pore structure and the straight-line length  $d_{straight-line}$  through the electrode, i.e. its thickness.

$$\tau_{geo} = d_{path}/d_{straight-line} \quad [1]$$

The geodesic tortuosity  $\tau_{geo}$  is a purely geometric descriptor, which is not adequate to determine the conductivity of the electrolyte inside the pores of the electrode. In particular, the bottleneck effect, i.e. the impact caused by the different pore sizes in electrodes, is not included in the descriptor  $\tau_{geo}$ . For this case, the implementation of a constriction factor  $\beta$  is necessary, which considers the bottleneck effect. Based on simulation studies using virtual but realistic microstructures, it was shown that the M-factor (the inverse of the MacMullin number  $N_M$ )<sup>25</sup> can be predicted with high accuracy by the electrode porosity  $\varepsilon$ , the geodesic tortuosity  $\tau_{geo}$ , and the constriction factor  $\beta$  as the ratio of the effective conductivity  $\kappa_{eff}$  to the intrinsic conductivity  $\kappa$  of the electrolyte.<sup>26</sup>

$$M = \frac{\kappa_{eff}}{\kappa} \approx \frac{\varepsilon^{1.15} \beta^{0.37}}{\tau_{geo}^{4.39}} \quad [2]$$

An alternative concept of tortuosity is the electric tortuosity  $\tau_e$ , which is defined by the alteration of the conductivity in a porous structure.<sup>21</sup>

$$\tau_e = \frac{\varepsilon}{M} = \frac{\kappa * \varepsilon}{\kappa_{eff}} \quad [3]$$

After a rearrangement of Eq. 3 using  $\kappa_{eff} = d/(A * R_{ion})$ , Eq. 4 is obtained, which allows an experimental determination of the electric tortuosity  $\tau_e$ .

$$\tau_e = \frac{R_{ion} * A}{d} * \kappa * \varepsilon \quad [4]$$

Equation 4 links the pore structure expressed by the tortuosity  $\tau_e$  with the ionic resistance  $R_{ion}$  of the electrolyte, which can be derived from EIS measurements.<sup>25,27,28</sup> The electrode area  $A$  and the electrode thickness  $d$  are geometric factors of the measured sample. Note, that in the following, the simplified notation  $\tau = \tau_e$  is used.

**Electrochemical impedance spectroscopy.**—In this work a symmetric cell setup with blocking condition is used. This condition is achieved by using a blocking electrolyte, that hinders a faradaic reaction as it cannot intercalate into the active material.<sup>25</sup> A low conductive salt concentration in the electrolyte increases the electrolyte resistivity and therefore diffusion effects inside the electrode pore structure.

Figure 2 shows a simulation of the equivalent circuit model (ECM), which is used in this investigation. It is mathematically derived with parameters, which are chosen in the same order of magnitude as the experimental data determined later. Three frequency regions are highlighted, representing different processes in the cell. The pure resistance  $R_{pure}$  is the sum of all only ohmic resistances such as cable and electrolyte resistance.<sup>25,28,29</sup> In the high-frequency region, which is represented by a resistor in parallel with a capacitor, a semi-circle is formed. In the majority of publications this is attributed to the contact impedance between current collector and electrode film.<sup>25,28,30–35</sup> Numerous influences are known to affect this semi-circle, e.g. the diameter depends on the current collector material,<sup>31,33,34</sup> carbon black content,<sup>33</sup> cell conditions (pristine, formatted, aged),<sup>30</sup> application of an external force to the cell,<sup>33</sup> and compaction of the electrodes by pressing before cell assembling.<sup>25,28</sup> Alternative explanations include influences of carbon binder domains (CBD)<sup>36</sup> and pore geometry.<sup>37,38</sup> Simulations also show the creation of a semicircle after changing the conductivity properties of the electrolyte inside the CBD.<sup>36</sup>

In the mid- and low-frequency region, the ion diffusion of the electrolyte in the electrode pore structure and polarization of the pore walls determine the impedance. When the ions penetrate the pore at low frequencies and polarize the entire pore wall, the impedance becomes purely imaginary.<sup>25,31,38–40</sup> The electrolyte resistance in the pore is represented by resistors and the interface between the electrolyte and the solid electrode by constant phase elements (CPE).<sup>25,30</sup> These elements are combined in a transmission line model (TLM) that describes the impedance of a porous electrode with cylindrical pores.

A postulation for the use of the transmission line model is given by Landesfeind et al.,<sup>41</sup> who showed that the electrical resistance  $R_{el}$  of the electrode is important for the validation of the TLM. The requirement to obtain  $R_{ion}$  from a Nyquist plot is that  $R_{el}/R_{ion} < 0.01$ . Only for such a case the simplified TLM is valid. Usually, compacted electrodes were used to reduce  $R_{el}$ .<sup>28,41</sup> For this reason, only the calendared electrodes were chosen for the determination of  $R_{ion}$  and  $\tau$ .

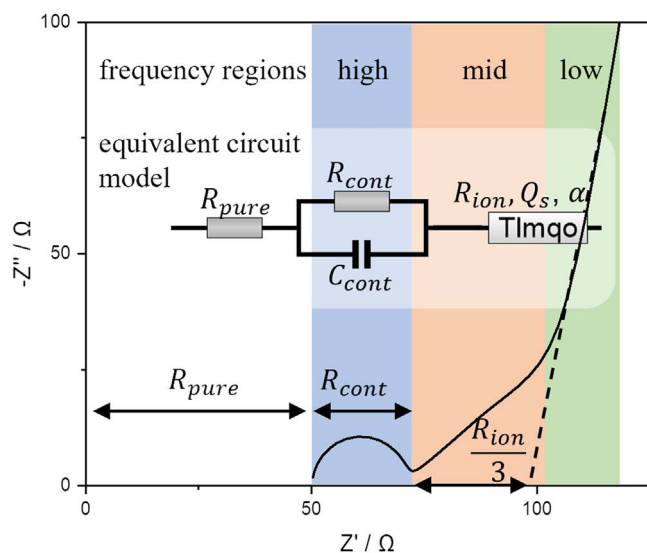


**Figure 2.** Equivalent circuit model with a simulated Nyquist plot for  $R_{pure} = 50 \Omega$ ,  $R_{cont} = 20 \Omega$ ,  $C_{cont} = 10^{-7} \text{ F}$ ,  $R_{ion} = 100 \Omega$ ,  $Q_s = 10^{-3} \text{ S s}^\alpha$ ,  $\alpha = 0.9$ .

The pore walls are polarized by an alternating current (AC) with different frequencies, which accelerates the ions in the liquid phase inside the pore (as described by Lasia<sup>42</sup>). The mathematical solution of such a case is given by Landesfeind et al.<sup>25</sup> and Lasia<sup>42</sup> with the pore impedance  $Z_{\text{pore}}$ , the surface impedance  $Z_s$ , the ionic resistance  $R_{\text{ion}}$ , the CPE quasi-capacity  $Q_s$ , and the CPE-exponent  $\alpha$ , which lies in a range from 0.5 to 1.

$$\begin{aligned} Z_{\text{pore}} &= \sqrt{R_{\text{ion}} Z_s} \coth \sqrt{\frac{R_{\text{ion}}}{Z_s}} \\ &= \sqrt{\frac{R_{\text{ion}}}{Q_s (i\omega)^\alpha}} \coth \sqrt{Q_s (i\omega)^\alpha R_{\text{ion}}} \end{aligned} \quad [5]$$

For higher frequencies the hyperbolic cotangent approaches 1 and after rearranging Eq. 5 simplifies to:

$$Z_{\text{pore}} = \sqrt{\frac{R_{\text{ion}}}{Q_s (i\omega)^\alpha}} = \sqrt{\frac{R_{\text{ion}}}{Q_s}} * (i\omega)^{-\frac{\alpha}{2}} \quad [6]$$

The first factor in Eq. 6 is a constant value whereas the second factor describes the real (Re) and imaginary (Im) contributions. The second factor is expressed in Eq. 7 by trigonometric functions, which allow the slope of the complex number to be examined in the complex plane.

$$(i\omega)^{-\frac{\alpha}{2}} = \left( \cos\left(\frac{\pi}{4} * \alpha\right) - i \sin\left(\frac{\pi}{4} * \alpha\right) \right) \quad [7]$$

The exponent  $\alpha$  indicates the deviation of the CPE from an ideal capacitor. At  $\alpha = 1$ , it becomes an ideal capacitor. In this case, the real and imaginary parts are equal, which means that they form a line with an angle of 45° in the Nyquist plot. If  $\alpha < 1$ , the imaginary part decreases in favor of the real part and the angle becomes smaller than 45°.

A different situation arises by considering the low-frequency section at  $\omega \rightarrow 0$ . With the series expansion for  $\coth(x)/x \approx 1/3 + 1/x^2$ , Eq. 5 becomes:

$$Z_{\text{pore}} = \frac{R_{\text{ion}}}{3} + \frac{1}{Q_s} * (i\omega)^{-\alpha} \quad [8]$$

Exact details of this conversion can be found at Lasia.<sup>42</sup> The impedance at low frequencies can be represented by a resistor and a capacitor in series. According to Eq. 8, the width of the mid-frequency region on the real axis can be assigned to  $R_{\text{ion}}/3$ . In the trigonometrical expression of the complex number

$$(i\omega)^{-\alpha} = \left( \cos\left(\frac{\pi}{2} * \alpha\right) - i \sin\left(\frac{\pi}{2} * \alpha\right) \right) \quad [9]$$

it can be recognized that for  $\alpha = 1$  the real part is zero and the imaginary part is  $-1$ . This means that the impedance is completely imaginary and is represented by a vertical element (90°) in the Nyquist plot. Physically, it is determined by its capacitive behavior. However, when  $\alpha < 1$ , the second term in Eq. 8 contains an additional real contribution and the slope decreases. As already shown, for  $\alpha = 1$ , the mid- and low-frequency region obtain an angle of 45° and 90° respectively, which corresponds to a factor of 2. It should be emphasized that this factor remains the same, even if  $\alpha < 1$ .<sup>31,43</sup>

## Experimental

**Material processing and characterization.**—A commercial  $\text{Li}(\text{Ni}_{1/3}\text{Co}_{1/3}\text{Mn}_{1/3})\text{O}_2$ , abbreviated NMC111 (NM-3100, Toda Kogyo Corp.) with compact particles (NCM-C) was used as reference material. These particles have a low proportion of non-accessible pores (Fig. 1). For the preparation of porous particles

(NCM-P), the powder was milled to submicron particle size, spray dried to form agglomerates similar to the original particle size, and calcinated at 850 °C in synthetic air for 5 h. The detailed processing route is described in Wagner et al.<sup>13</sup> and Müller et al.<sup>15</sup>

For particle characterization, the following instruments were used: Particle size distribution was measured by laser diffraction dispersed in 2-propanol (Horiba LA950, Retsch Technology), specific surface by BET method with  $\text{N}_2$  adsorbing gas (Gemini VII 2390, Micromeritics), true density by helium pycnometry (AccuPyc 1330, Porotec). Measured particle properties are shown in Table I. The primary particle size is defined as the mean size of individual crystallites within the particles, measured by image analysis as described in the electrode characterization chapter, while the secondary particle size represents the overall size of the particles.

**Slurry and electrode preparation.**—The slurries were mixed in a dissolver (Dispermat SN-10, VMA Getzmann) with 3.57 wt% carbon black (C65, Imerys), 3.57 wt% graphite (KS6L, Imerys), 3.57 wt% PVDF (5130, Solvay) binder, and 89.3 wt% NMC111 active material with the solvent N-Methyl-2-pyrrolidone (NMP, Carl Roth). The slurry had a solid content of 50.5 wt%. The electrodes were coated with a doctor blade on a 20  $\mu\text{m}$  aluminum foil that was pinned on a temperature-controlled plate. The electrodes were dried in a batch-wise working impingement dryer that allowed to set defined drying rates.<sup>20</sup> The isothermal drying temperatures for the drying rates 0.75, 1.5 and 3.5  $\text{g m}^{-2} \text{s}^{-1}$  were 61, 73 and 85 °C respectively (Eq. S4). Due to different electrode thicknesses, the mass loading varies from 10 to 16  $\text{mg cm}^{-2}$  for NCM-C and 10 to 18  $\text{mg cm}^{-2}$  for NCM-P. The calculation of the drying rate is shown in Eq. S4 in the supporting information. The final electrode porosity was set by calendaring between heated rolls at 50 °C (Saueressig GLK 200).

**Electrode characterization.**—The porosity was calculated from the electrode density (derived from electrode thickness and weight after compensation of the aluminum foil) divided by the true density of the electrode, which is 3.97  $\text{g cm}^{-3}$  and 4.08  $\text{g cm}^{-3}$  for NCM-C and NCM-P respectively (Eq. S2). The electrode thickness was measured by a length gauge (MT 12B, HEIDENHAIN) with a precision of  $\pm 0.5 \mu\text{m}$ . The average of 3 measurements was used. The pore size distribution of the electrodes was measured with Mercury intrusion porosimetry (Pascal 440 Evo, Thermo Scientific). Porosimetry was done with attached aluminum current collector, which was considered for porosity calculation as described in Froboese et al.<sup>44</sup> SEM cross-sections of the electrodes were prepared by ion-beam milling (EM TIC3X, Leica Microsystems) in a field-emission scanning electron microscope (Supra 55, Zeiss). The cross-sections were also used for the determination of the primary particle size by image analysis (ImageJ software) from more than 500 particles. The specific volume resistance of the electrodes at different porosities were measured between polished copper cylinders (diameter 14 mm) with an applied force of 1 kg and a milliohm meter in DC mode (RM3544, Hioki E.E. Corp.).

**Impedance spectroscopy measurements.**—CR2032 coin cells were assembled in a glove box (MBraun) with  $\text{O}_2$  and  $\text{H}_2\text{O}$  concentrations  $< 0.5 \text{ ppm}$  to a symmetrical cell set up with one spacer for each electrode and two glass fiber separators (GF/C, Whatman) per cell. 200  $\mu\text{l}$  of 10 mM tetrabutylammonium perchlorate  $\text{TBAClO}_4$  in EC:DMC (1:1 by volume) electrolyte (VWR International; Huntsman, Sigma Aldrich, respectively) was added. The conductivity  $\kappa$  of this electrolyte is  $(0.3487 \pm 0.0024) \text{ mS cm}^{-1}$  and  $(0.3505 \pm 0.0011) \text{ mS cm}^{-1}$  (two batches were used). Electrodes and separators were punched out with a diameter of 1.6 cm corresponding to an area  $A = 2.01 \text{ cm}^2$ . EIS measurements were performed in a temperature-controlled chamber (BTZ-175, Espec) at 25 °C using a coin cell holder (Dual CR2032 Coin Cell Holder, Gamry Instruments) with a potentiostat (VSP-300, Biologic). The measuring parameters were 10 mV perturbation, a frequency range

**Table I. Particle properties of compact NCM-C and porous NCM-P.**

	Primary particle size $\mu\text{m}^{-1}$	Pristine/secondary particle size $\mu\text{m}^{-1}$	Specific surface area/ $\text{m}^2 \text{g}^{-1}$	True density/ $\text{g cm}^{-3}$	Secondary particle porosity/—
NCM-C	0.770	7.3	0.4	4.52	—
NCM-P	0.434	10.0	2.9	4.70	0.476

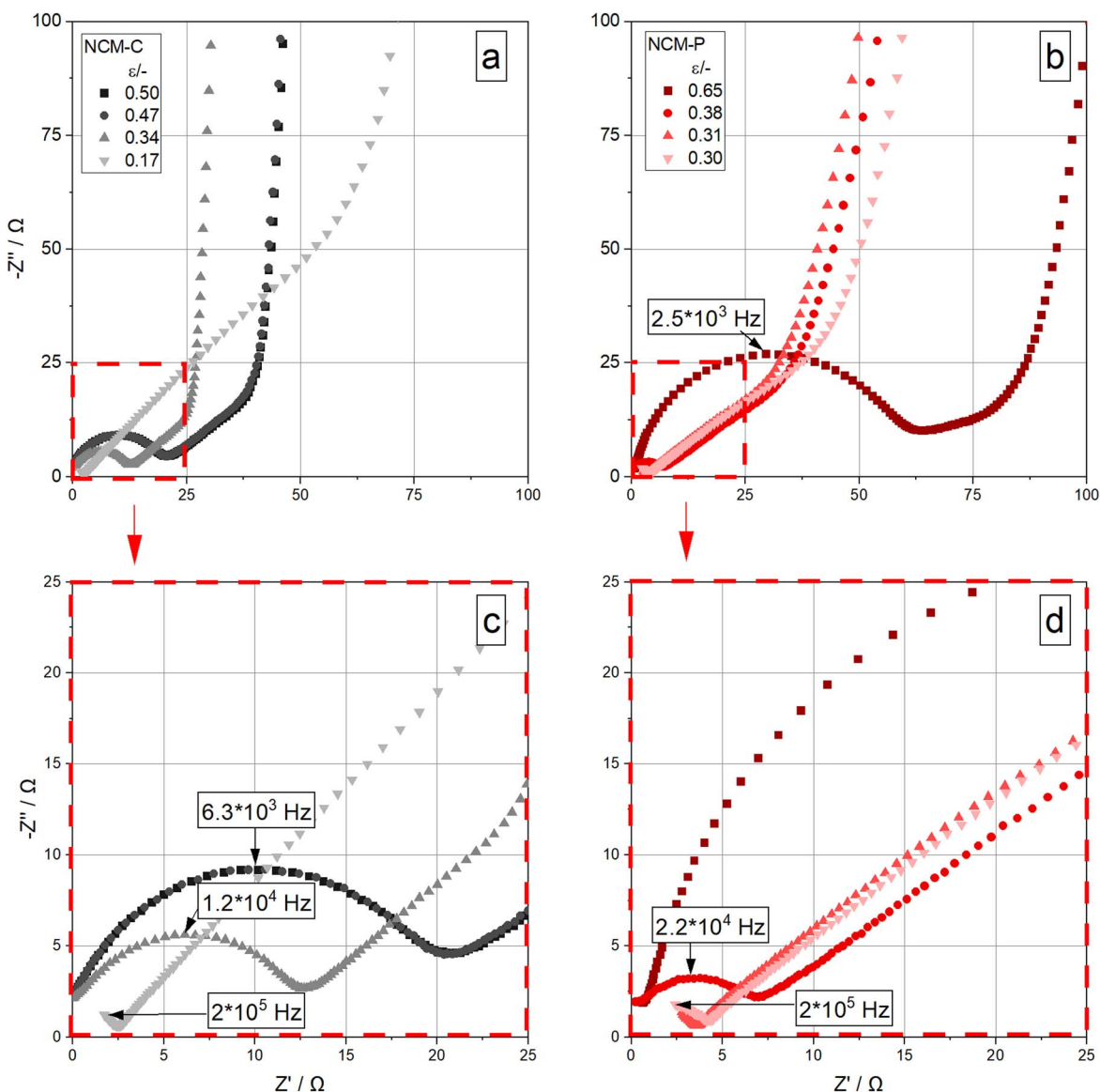
from 200 kHz to 100 mHz and 20 points per decade. A preliminary examination revealed a time-dependent impedance behavior of fresh cells, which remained constant after one day (Fig. S1). Thus, all presented graphs, fit parameters, and further calculations were taken from the day after cell preparation. The obtained EIS data were plotted and fitted in an EIS software (RelaxIS 3, rhd instruments) by using the equivalent circuit model described in the theory section. For better comparability of the Nyquist plots, the real part is normalized to  $R_{\text{pure}}$  in the following.  $R_{\text{pure}}$  is  $(62 \pm 9) \Omega$  for all measured cells. A huge impact on  $R_{\text{pure}}$  has the electrolyte conductivity (Fig. S2).

## Results

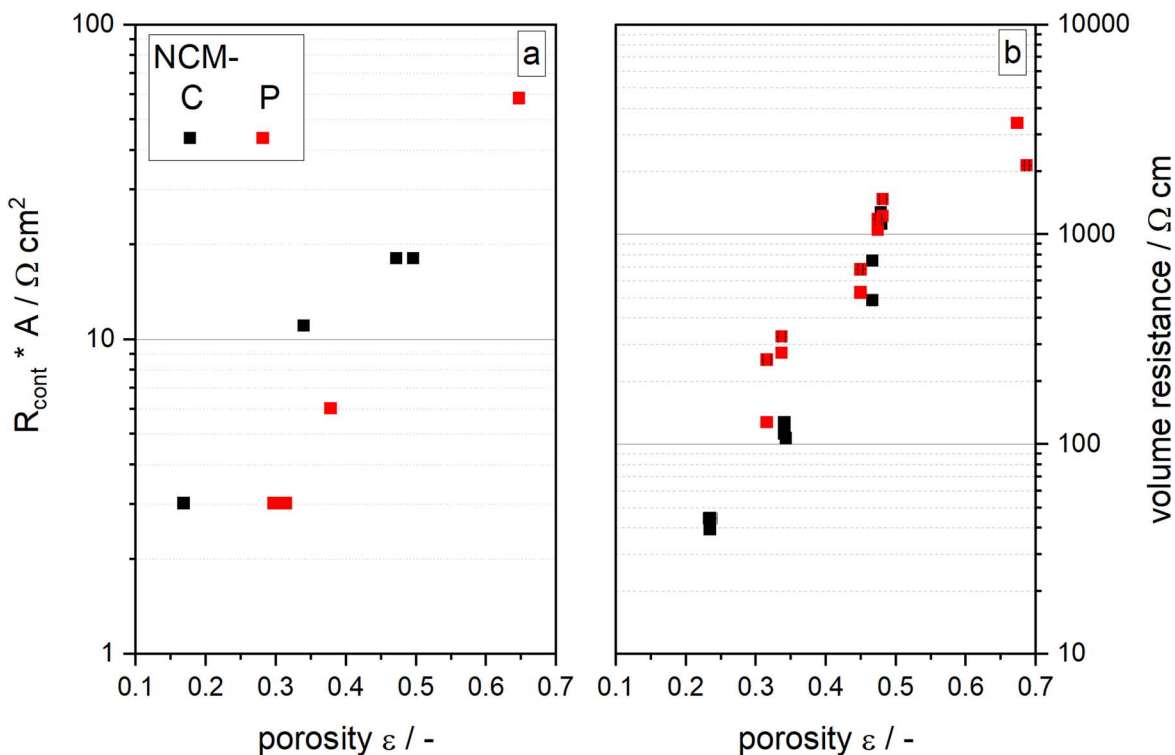
**Electrical resistance.**—Figure 3 shows the Nyquist plots of NCM-C (a, c) and NCM-P (b, d) cathodes at different porosities  $\varepsilon$  depicting the typically course of such a cell setup (compare to Fig. 2). In the non-calendered state after electrode coating, the electrodes have the highest  $\varepsilon$ , which depends on the active material particles. In Fig. 3 the highest  $\varepsilon$  is 0.5 for NCM-C and 0.65 for NCM-P. The electrodes with NCM-P have a significantly higher porosity because of their intragranular porosity. The non-calendered electrodes show a large semicircle in the high-frequency region,

which decreases for both particle systems by calendering. At high compaction and low porosity, the semicircles are incomplete due to the upper frequency limit and can therefore only be estimated. This effect can also be seen in the Bode plot, where a shift to higher frequencies is visible with the peaks partly moving out of the observed frequency range (Fig. S3). At a comparable porosity of 0.38, the semicircle for the NCM-P electrode is smaller because a higher compression was necessary to reach this level. Pritzl et al. made an estimation of the double layer capacity, which should be in the order of  $10 \mu\text{F cm}^{-2}$ .<sup>33</sup> Transferring the approach to this work and repeating the calculations gives a capacity of  $0.3 \mu\text{F cm}^{-2}$  for using the area of the current collector or ca.  $7 \cdot 10^{-5} \mu\text{F cm}^{-2}$  for the BET surface of NCM+CB. It is obvious that the double layer capacity calculated from the current collector area is much closer to the expected value of  $10 \mu\text{F cm}^{-2}$ . This gives an indication that the observed semi-circle in the high-frequency region represents the impedance of the interface between the current collector and the electrode film and  $R_{\text{cont}}$  obtained by a fit of the EIS results from Fig. 3 with the ECM shown in Fig. 2 can be assigned to the contact resistance between current collector and electrode film.

In Fig. 4a,  $R_{\text{cont}}$  is normalized to an area resistivity by multiplication with the electrode area  $A$  and plotted as a function of porosity  $\varepsilon$ . The initial areal resistivity  $R_{\text{cont}} \cdot A$  for the non-



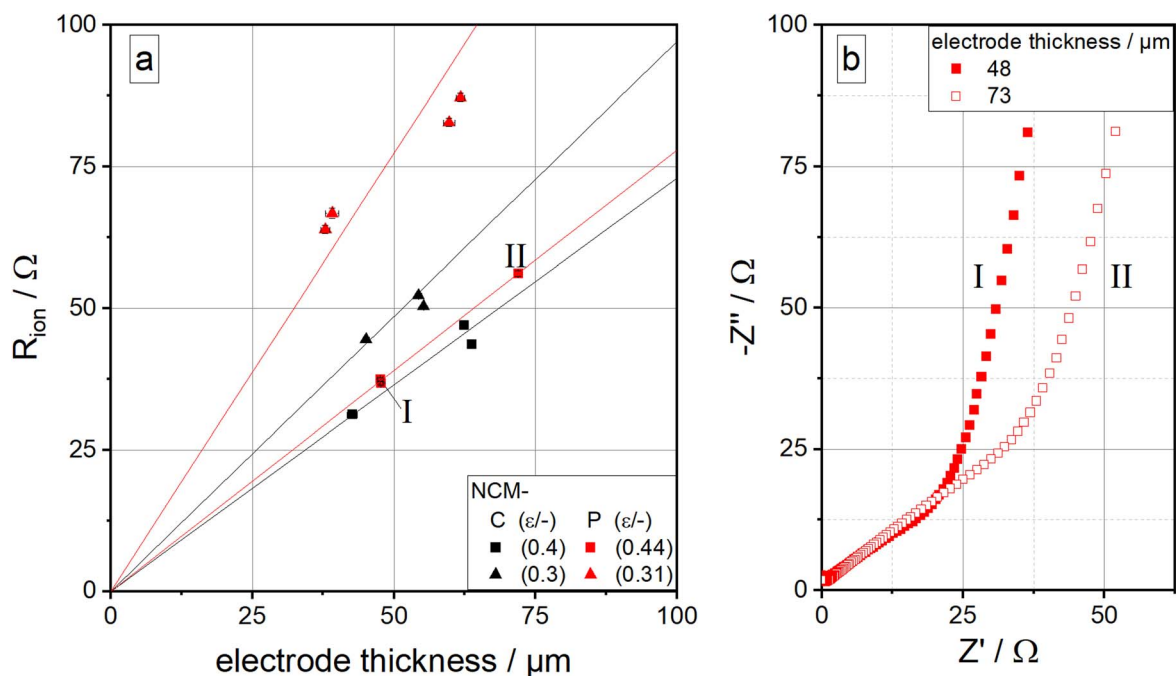
**Figure 3.** Nyquist plots of NCM-C (a), (c) and NCM-P (b), (d) at different porosities. Magnified areas from the overview graphs are shown in (c) and (d).



**Figure 4.** Specific areal and volume resistances over the electrode porosity. Areal resistance  $R_{\text{cont}} * A$  (a) is determined from EIS and specific volume resistance (b) is measured by an ohmmeter.

calendered electrode is higher for NCM-P as for NCM-C.  $R_{\text{cont}} * A$  decreases by calendering from  $20 \Omega \text{ cm}^2$  to  $2 \Omega \text{ cm}^2$  for NCM-C and from  $60 \Omega \text{ cm}^2$  to  $2 \Omega \text{ cm}^2$  for NCM-P. Similar porosity-dependent  $R_{\text{cont}}$  decreasing was shown systematically by Landesfeind et al.<sup>25</sup> for lithium iron phosphate cathodes. The importance of calendering for  $R_{\text{cont}}$  becomes obvious once again at this point. Despite of the higher  $R_{\text{cont}}$  in the non-calendered state for NCM-P, both particle morphologies result in a comparable  $R_{\text{cont}}$  at lower porosities.

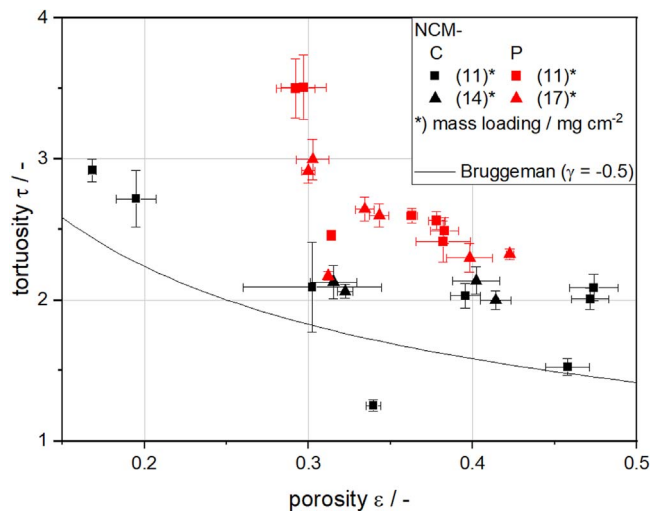
For a classification of  $R_{\text{cont}} * A$ , the overall ohmic resistance of the electrodes was also measured between copper cylinders by an ohmmeter. The specific volume resistance is plotted as a function of the porosity in Fig. 4b. The volume resistance is again higher for the non-calendered NCM-P than for NCM-C. Müller et al. describe that compaction by calendering leads to a higher number of contact points of the particles within the electrode, which reduces the electrical resistance. At the same time, the NCM particles are



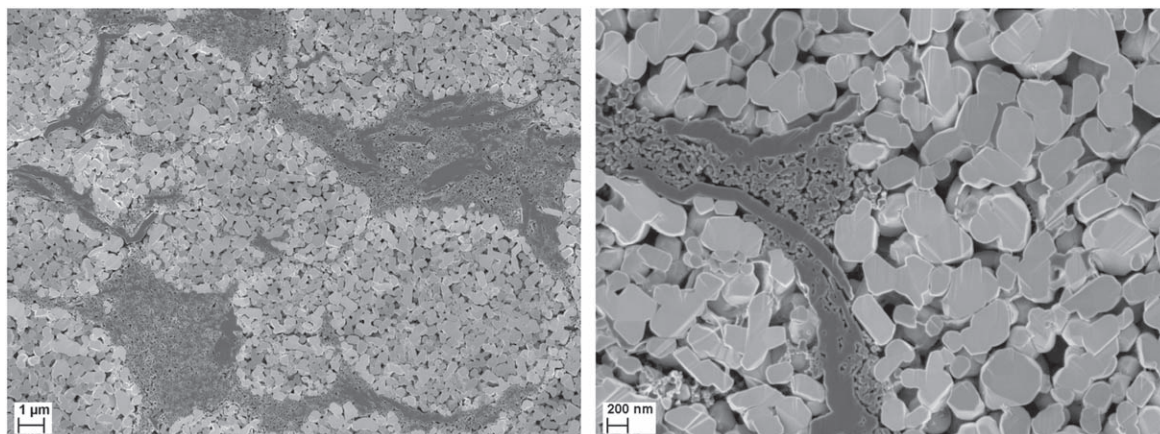
**Figure 5.**  $R_{\text{ion}}$  as a function of electrode thicknesses (set by various mass loadings and porosities) for NCM-C and NCM-P (a). Nyquist plots of exemplary NCM-P electrodes with porosity  $\epsilon = 0.44$  at different electrode thickness (b).

**Table II.** Specific ionic resistance  $\rho_{\text{ion}}$  (calculated by Eq. 10) at different porosities and particle morphologies.

	Porosity $\varepsilon$ / -	Specific ionic resistance $\rho_{\text{ion}} / \Omega \text{ cm}^2 \mu\text{m}^{-1}$
NCM-C	0.4	1.47
	0.3	1.97
NCM-P	0.44	1.57
	0.31	3.11

**Figure 6.** Tortuosity as a function of porosity for NCM-C (black) and NCM-P (red). The Bruggeman curve is calculated with  $\tau = \varepsilon^{-\gamma}$ .<sup>41</sup>

pushed into the aluminum current collector, increasing the contact area and thus the contact resistance decreases.<sup>15</sup> Sim et al. showed in a calendaring study for electrodes with  $\text{LiNi}_{0.90}\text{Mn}_{0.05}\text{Al}_{0.05}\text{O}_2$  that the  $R_{\text{cont}}$  is decreasing from 35 to 0  $\Omega \text{ cm}$ .<sup>45</sup> The volume resistance is the total resistance of the electrode, which includes the bulk resistance of the electrode film itself and the contact resistance between the electrode and the current collector. While  $R_{\text{cont}}$  is related to the electrode area, the volume resistance is related to the electrode volume. Therefore, the absolute values cannot be compared directly. However, the reduction in resistance due to reduction in porosity is of similar percentage magnitude for both measurements. This indicates that  $R_{\text{cont}}$  has a dominant influence on the total resistance measured with an ohmmeter and that a total volume resistance of the electrode is not equal to the volume resistance of the electrode.

**Figure 7.** SEM images of the cross-section of strongly calendared NCM-P electrodes ( $\varepsilon \sim 0.4$ ).

**Ionic resistance.**—Theoretically, the ionic resistance  $R_{\text{ion}}$  is linearly correlated with electrode thickness  $d$ , specific resistance  $\rho$ , and electrode area  $A$  by Eq. 10.

$$R = \frac{\rho d}{A} \quad [10]$$

This was verified with electrodes coated from the same slurry at different thicknesses, calendared and analyzed by EIS. The Nyquist plot in Fig. 5b shows exemplary results with an increased extension of the mid-frequency region, which correlates with  $R_{\text{ion}}$ . The dependence of  $R_{\text{ion}}$  to electrode thickness is shown in Fig. 5a. Electrodes with different coating thicknesses follow Eq. 10, i.e. the ionic resistance is proportional to the electrode thickness. However, after reducing the porosity by calendaring, the slope of the best-fit line changes and so does the ionic resistivity. The corresponding specific ionic resistances  $\rho_{\text{ion}}$  calculated from Fig. 5a by Eq. 10 are shown in Table II. It indicates that the ionic resistance of NCM-P is also more affected by calendaring.

**Tortuosity.**—The increasing ionic resistance can be attributed to the change of the pore structure by the calendaring process. This is also expressed by the electrical tortuosity (derived from Eq. 4) as a function of the porosity in Fig. 6. The EIS measurements lead to higher values for tortuosity compared to the simple Bruggeman estimation. Electrodes with NCM-P particles have a higher tortuosity than NCM-C. While there is only a moderate increase in tortuosity for NCM-C by calendaring, it increases strongly for NCM-P at a porosity of around 0.3. The minimum porosity achieved by calendaring was 0.17 for NCM-C and 0.29 for NCM-P. NCM-C follows the Bruggeman trend,<sup>41</sup> although with higher values. Even after strong densification, an intergranular porosity exists around the compact particles, which can be used for the ion transport. The pore structure for the NCM-P particles differs significantly from this. The porous particles already have an intragranular porosity of 0.47. A closer look at the porosity shows that electrodes with NCM-P have two porosity fractions. The calculation of the porosity for the intra- and intergranular pores is described in the supporting information (Eq. S1 and Eq. S2). Starting with non-calendared electrodes, the intragranular porosity is about 0.25 and the intergranular porosity is 0.4 (which is 0.65 overall for the total electrode porosity). Assuming that the intragranular porosity is constant during calendaring, the intergranular porosity of electrodes with NCM-P shrinks from 0.4 to 0 with a total porosity of 0.25. However, this estimate is only accurate for non-calendared electrodes where the intragranular porosity is known. With massive calendaring, the intergranular porosity values can become negative with this approximation. This indicates that the porous particles are also compressed for high electrode compression. Müller et al. demonstrated the apparent quasi-plastic deformation of the porous particles by calendaring,

enabling a substantial reduction of the intergranular pores.<sup>15</sup> The resulting microstructure can be seen in Fig. 7 presenting SEM images of massively calendared electrodes. The cross-sections show the porous NCM-P particles and the CBD between them. At high compression, the intergranular pores are eliminated or completely stuffed with the CBD. Shodiev et al. show in simulations that the ionic resistance inside the CBD is very high compared to the free pore phase.<sup>36</sup> If the CBD covers more of the intergranular pore space, the ionic resistance, and thus, the tortuosity should rise.<sup>46,47</sup> In this work, the CBD has a smaller pore size than the intragranular pores of the NCM-P (Fig. 7). This forces a high number of ions to diffuse through the intragranular NCM pores. The resulting diffusion paths are extended and therefore the ionic resistance and tortuosity. In addition, the conductive graphite, which is a component of the CBD, hinders ion transport due to its impermeable platelet structure. As a result, the tortuosity of NCM-P increases when the intergranular pores are more and more occupied by the CBD. When completely filled, further compaction must take place via a reduction of the intragranular porosity. In this case, the transport paths through the NCM-P particles will also be clogged and the tortuosity strongly increases. According to Fig. 7, the point, where the intergranular porosity is eliminated is located at a porosity of around 0.3.

**Pore structure considerations.**—In the mid- and low-frequency region of the Nyquist plot, ion diffusion of the electrolyte in the pore structure and pore wall polarization are determining the impedance of the electrode. As discussed in the theory section, this leads to a theoretical angle of 45° and 90° in the mid- and low-frequency range respectively, with both slopes interconnected by a factor of 2. Differences from the theoretical gradients can be attributed to the  $\alpha$  value in the CPE of the TLM revealing a deviation from an ideal capacitor. In literature, data to  $\alpha$  are rare and not investigated systematically for LIB. Wang et al. examined various active materials in symmetric cells.<sup>28</sup> A range from 0.87 to 0.96 was found for  $\alpha$  for different materials like LFP, NCM, LTO, LCO and different particle morphology and diameter. However, mass loading, porosity, and formulation was also varied so that a correlation between particle morphology and  $\alpha$  cannot be derived.<sup>28</sup>

In Table III, the results from all measured electrodes (excluding non-calendared and high drying rate electrodes) and the ratios between low to mid-frequency slopes are summarized as mean values. In general,  $\alpha$  and the slopes in the mid- and low-frequency regions are lower than the theoretical values and lower for NCM-P than for NCM-C. A non-ideal behavior ( $\alpha < 1$ ) is basically caused by a distribution of time constants.<sup>42</sup> There are three major differences regarding the surface polarization process of compact vs porous particles that could influence  $\alpha$ :

1. The contribution of the surface of NCM particles to the overall BET surface area in the electrodes is about 10% for NCM-C and 50% for NCM-P (calculated from Eq. S1). Since the polarization behavior between a good (i.e., conductive carbon) and a bad electron conductor (i.e., NCM) is different, the NCM contribution to the overall surface affects  $\alpha$ . Due to the larger contribution, a larger deviation occurs for NCM-P.
2. For NCM-C particles, a larger fraction of the surface has direct contact to the conductive CBD. For NCM-P particles, only primary particles in the outer shell are electrically connected

with CBD leading to a distribution of the polarizable surface within the porous particles.

3. The ionic resistance is different for intergranular or intragranular pores due to the dissimilar pore sizes. Giving the pore size distributions in Fig. 10, the higher ionic resistance of the intragranular porosity should lead to a larger deviation of  $\alpha$  for NCM-P.

It is hardly possible to identify the actual impact leading to a lower  $\alpha$  for NCM-P. However, some results in literature provide hints that the first effect might be the most relevant. Oswald et al. increased the surface of electrodes by cracking NCM622 particles during calendaring. Consequently, the electrode double layer capacitance increases, as the specific surface area is increasing. This leads to a shrinking  $\alpha$ . Furthermore, pure carbon fiber electrodes show an  $\alpha = 0.97$ , but the more the surface of NCM622 in a normal electrode increases, the lower gets  $\alpha$ .<sup>48</sup>

Exemplary Nyquist plots for NCM-C and NCM-P are shown in Fig. 8. NCM-C shows good agreement with the fit from the TLM, while NCM-P does not show the same angle and stronger deviations from a straight line in the mid-frequency region. Consistent to this, the slope ratio also shows a strong deviation from the theoretical value of 2 for NCM-P, while it agrees for NCM-C (Table III). Cooper et al. show in simulations that the mid-frequency region in the Nyquist plot is influenced by the structure of the pore network. A more branched pore network compared to a cylindrical pore leads to a curved mid-frequency range with low slope.<sup>37</sup> Nguyen et al. studied a pore through the electrode with additional different dead-end pores at the main pore. These dead-end pores also lead to a curved shape in the mid-frequency region.<sup>38</sup> This explains the larger deviation for the more branched pore structure of the NCM-P electrodes, where the resistance of the ions to reach the solid/liquid surface is higher than for NCM-C electrodes.

These results show that the transport behavior in the electrode is generally deteriorated by using NCM-P instead of NCM-C. Although in a moderate porosity range around  $\varepsilon = 0.35$ – $0.45$ , the increase in tortuosity is only about 25%, at lower porosities the tortuosity of NCM-P so strongly increases that at one point a significant reduction of the cell performance can be expected. In conclusion, the pore structure of NCM-P has a negative effect on the transport properties of the electrode. Since NCM-P has improved rate capability compared to NCM-C this must be attributed to different factors than the more extended pore structure.

**Variation of drying rate.**—The pore morphology has a massive influence on the drying behavior of electrodes, in particular on the binder migration, which is usually favored at high drying rates.<sup>49,50</sup> Previous publications have shown that this has a much stronger effect on the adhesion strength, volume resistance and rate capability of electrodes with NCM-C than those with NCM-P.<sup>20</sup> Müller et al.<sup>15</sup> and Klemens et al.<sup>20</sup> suggested that the lower binder concentration at the interface between electrode and current collector is the reason for a higher ohmic resistance of the electrodes, although the explicit contribution of the interface could not be measured directly. This statement becomes plausible when considering that the binder is normally associated with conductive carbon black in a CBD. In this work, a separate acquisition of the contact resistance  $R_{\text{cont}}$  is made possible, which supports the hypothesis. In the non-calendared state,

**Table III. Mean values of  $\alpha$  and angles of mid-/low-frequency regions and the ratio between them for NCM-C and NCM-P.**

	$\alpha$	Angle $\chi^\circ$		Angle ratio $\chi_{\text{low}}/\chi_{\text{mid}}$
		Mid frequency	Low frequency	
TLM (theory)	1	45	90	2
NCM-C	0.960 ± 0.008	42.6 ± 1.7	85 ± 1	2.00 ± 0.09
NCM-P	0.91 ± 0.01	35.9 ± 1.5	81.9 ± 1.4	2.29 ± 0.12

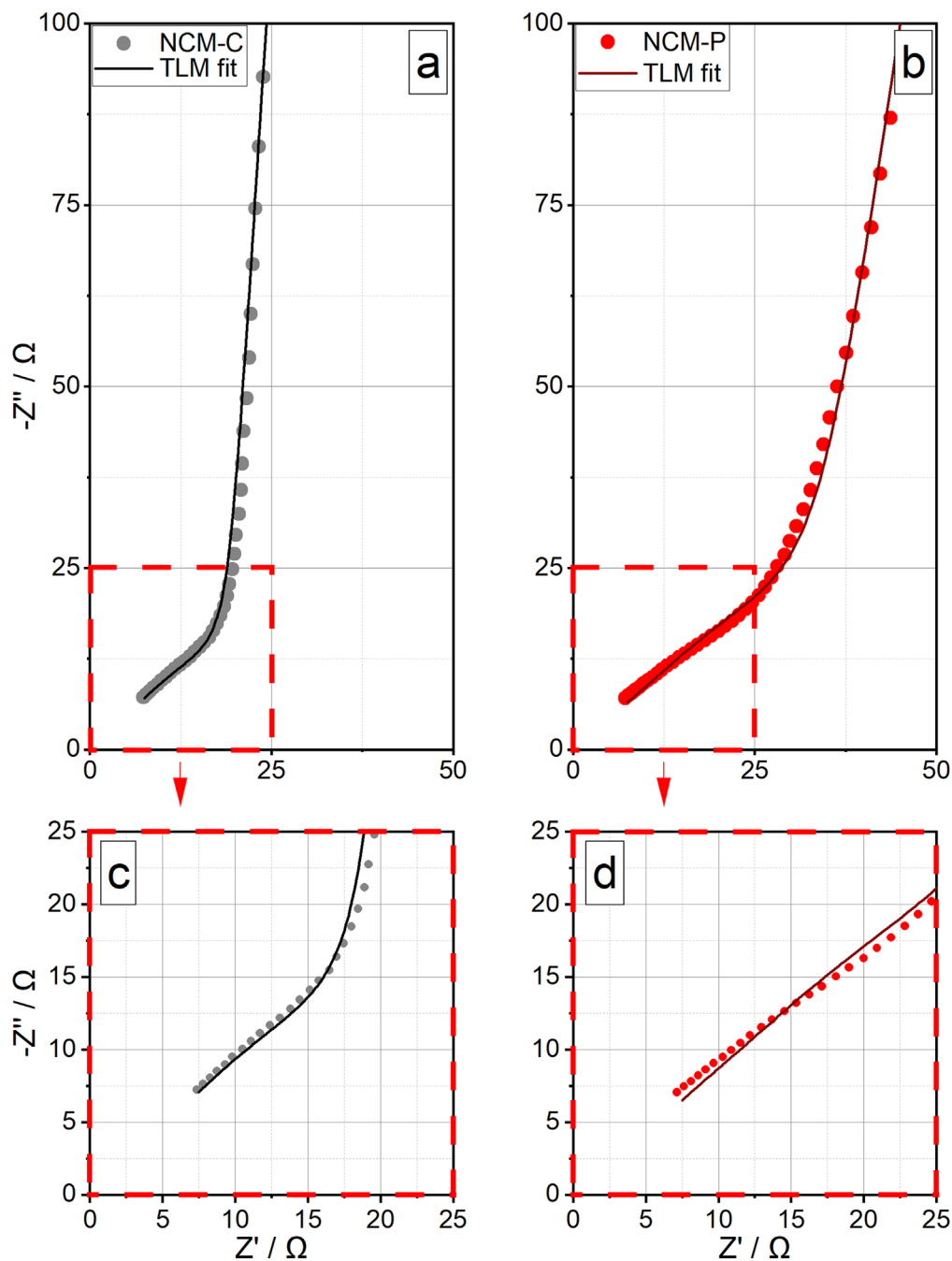
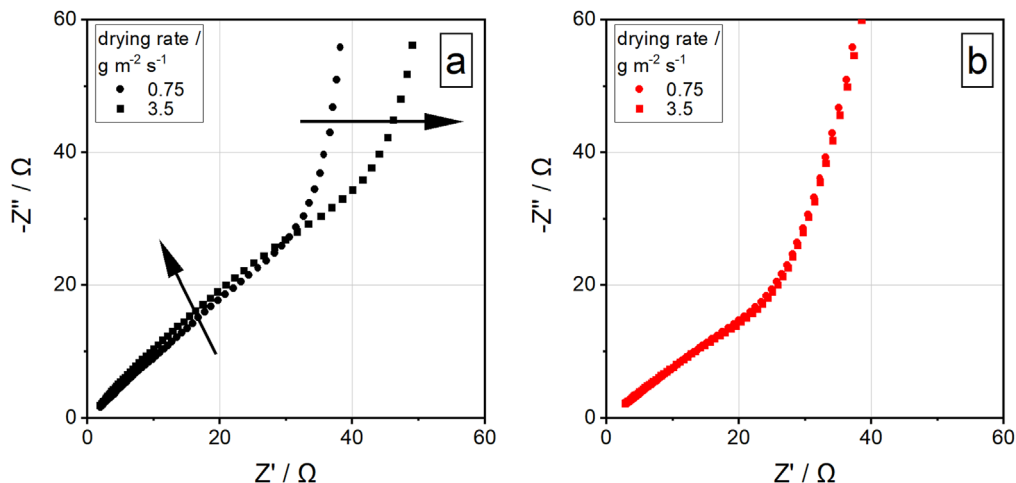


**Figure 8.** Nyquist plot from NCM-C (a), (c) and NCM-P (b), (d). These plots are a section of the entire measurement, which is shown in Fig. S4.

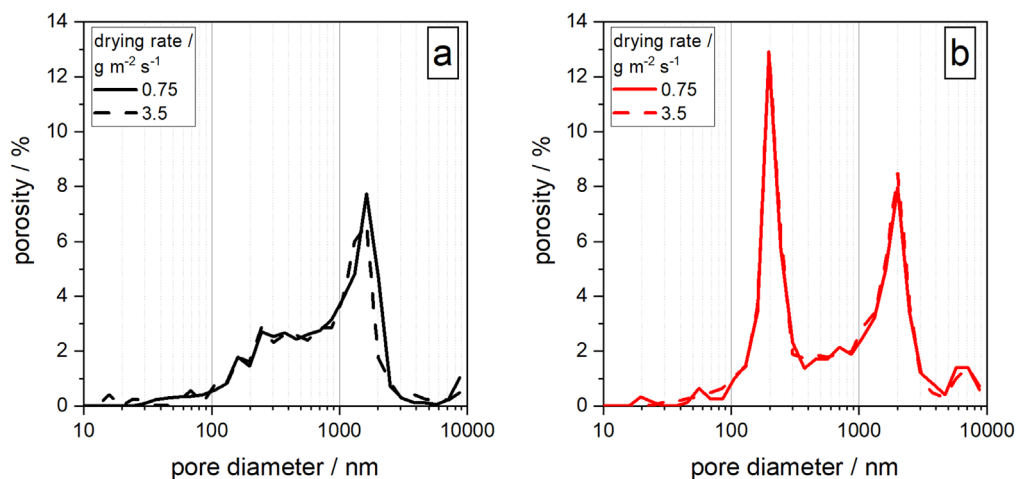
$R_{\text{cont}} * A$  increases from  $19 \Omega \text{ cm}^2$  at a drying rate of  $0.75 \text{ g m}^{-2} \text{ s}^{-1}$  to  $35 \Omega \text{ cm}^2$  at a drying rate of  $3.5 \text{ g m}^{-2} \text{ s}^{-1}$  for NCM-C, while it rises from  $60 \Omega \text{ cm}^2$  to  $100 \Omega \text{ cm}^2$  for NCM-P (Fig. S5). After calendaring  $R_{\text{cont}} * A$  decreases to the range of  $3$  to  $5 \Omega \text{ cm}^2$  for both particle morphologies and drying rates. The improved direct contact between electrode particles and current collector can overcome the binder impact. However, the electrical resistance cannot explain the rate capability results e.g. for calendared NCM-C electrodes as despite similar resistivity the 5C capacity at the high drying rate was  $\sim 63\%$  lower as for the low drying rate.<sup>20</sup>

Figure 9 shows a comparison of Nyquist plots for two different drying rates. The mid-frequency region for NCM-C electrodes is extended and is more curved at a drying rate of  $3.5 \text{ g m}^{-2} \text{ s}^{-1}$  compared to  $0.75 \text{ g m}^{-2} \text{ s}^{-1}$ . In addition, the shoulder of the phase angle in the Bode plot shifts to lower frequencies (Fig. S6). These

phenomena are first described by Morasch et al.<sup>51</sup> in a simulated gradient-TLM for a graphite anode. According to them, a binder gradient along the electrode thickness leads to an enlarged mid-frequency region and extended curvature, while in the Bode plot the shoulder peak should become larger.<sup>51</sup> Nguyen et al. simulated pore structures where the top of the electrode (next to the separator) has a lower porosity than the rest of the electrode.<sup>38</sup> This is the case when the binder migrates to the top of the electrode and reduces the local porosity because it accumulates and clogs the pore space. Thus, all ions which migrate into the electrode are hindered by this upper layer and this also leads to an enlarged curvature in the mid-frequency region. Evidence for the formation of such a top layer with reduced porosity could be revealed by Mercury porosimetry only for NCM-C by a moderate peak shift at a pore diameter of



**Figure 9.** Nyquist of electrodes with NCM-C (a) and NCM-P (b) at the drying rates 0.75 and 3.5  $\text{g m}^{-2} \text{s}^{-1}$  and a porosity of  $0.303 \pm 0.014$  for NCM-C and  $0.383 \pm 0.015$  for NCM-P.



**Figure 10.** Hg intrusion porosimeter distribution of non-calendered electrodes with NCM-C (a) and NCM-P (b) at drying rate 0.75 (lined) and 3.5  $\text{g m}^{-2} \text{s}^{-1}$  (dashed).

around  $1.5 \mu\text{m}$  although the difference is not very significant (Fig. 10a).

For NCM-P electrodes (Fig. 9b), no comparable changes of the Nyquist plots were detectable at both drying rates. In addition, the entire porosity of the NCM-P electrodes isn't significantly influenced by the drying rate (Fig. 10b).<sup>52-54</sup> Therefore, it can be assumed that increasing the drying rate does not change the microstructure for NCM-P electrodes or create an ion impeding layer by binder migration. This result explains why no dependence of the rate capability on the drying conditions was determined for these electrodes up to 5C.<sup>20</sup>

To quantify the transport phenomena influenced by binder migration, the M-factor calculated according to Eq. 3, which integrates porosity and tortuosity, is plotted against the drying rate in Fig. 11. For the low drying rate, NCM-C has a slightly higher M factor than NCM-P. However, the M factor of NCM-C decreases much more when the drying rate is increased. The M-factor directly relates to the electrolyte conductivity  $\kappa^{\text{eff}}$  inside the pore structure of the electrode (Eq. 2), such that  $\kappa^{\text{eff}}$  decreases by 30% for NCM-C and only 10% for NCM-P by increasing the drying rate from 0.75 to 3.5  $\text{g m}^{-2} \text{s}^{-1}$ . Therefore, it can be assumed that the main reason for the worse cell performance of NCM-C electrodes at higher drying rates<sup>20</sup> can be attributed to the increased ionic resistivity of the pore structure caused by binder migration and inhomogeneous binder distribution.

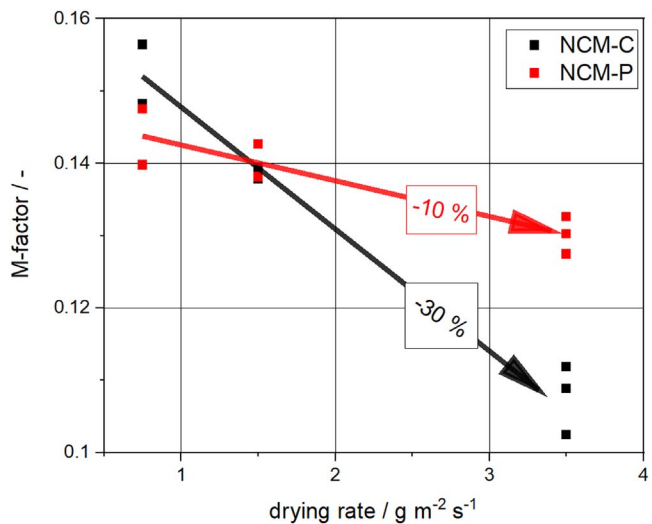


**Figure 11.** M-factor as a function of drying rate for NCM-C and NCM-P. The drying rates for the electrodes were 0.75, 1.5 and 3.5  $\text{g m}^{-2} \text{s}^{-1}$ . The porosity is 0.30 for NCM-C and 0.38 for NCM-P.

## Conclusions

Porous particles show improved rate capability compared to compact particles. This was attributed to shorter diffusion paths and an enlarged active surface area between the active material and the electrolyte, while the influence of the complex pore structure of the respective electrodes was unknown. In this work, electrochemical impedance spectroscopy (EIS) of symmetrical cells under blocking conditions is used to study resistance characteristics such as the contact resistance between the current collector and the electrode film, and the ionic resistance within the pore structure of the electrode. The measured impedance spectra can be described by a resistor in parallel with a capacitor which represents the contact impedance between the current collector and the electrode film. In series, a transmission line model with a constant phase element describes the impedance of the pore structure and pore walls.

During calendaring the contact resistance decreases in accordance with the ohmic resistance of the investigated NCM111 electrodes. However, the results of the EIS measurements indicate that there is a stronger reduction of the contact resistance for porous particles. In contrast to the contact resistance, the ionic resistance of the electrodes increases by calendaring, and the effect is also more pronounced for porous particles than for the compact ones. The reason for this effect is a change of the pore structure that can also be expressed by an altered electrical tortuosity. A moderate increase of the tortuosity takes place with compact particles, as the pore size is reduced but an opened pore system exists even at high densification to a porosity of 0.17, which can be used for the ion transport. It thereby follows the Bruggeman trend, albeit at higher values. In contrast to this, the tortuosity strongly rises at a porosity of around 0.3 for the porous particles as the pore structure for porous particles differs significantly. The porous particles already have an intragranular porosity of 0.47, which is quite resistant to further compaction. Getting to same porosity as for electrodes with compact particles, the intergranular pores must be sufficiently compressed. Electrodes with porous particles therefore have a higher tortuosity as for compact particles at the same electrode porosity. Due to the quasi-plastic deformation behavior of the porous particles, it is possible to densify the intergranular pores until they are eliminated, or they only contain carbon black-binder-domains (CBD). In this state, further densification of the electrodes is hardly feasible, only leading to increasing ionic resistance and tortuosity. As a consequence, it can be concluded that even massive densification of electrodes with compact particles only moderately increases the ionic resistance, whereas it is not possible for the porous particles to achieve extremely low electrode porosity without massively increasing the ionic resistance of the electrodes. From the view of the transport properties in the electrolyte, the usage of porous particles offers therefore no benefit.

The EIS measurements can also provide an explanation for the different electrochemical properties at high drying rates. Binder migration results to a depletion of binder and carbon black at the interface to the current collector and to an accumulation of this components at the side to the separator. This leads to an increased contact resistance at the interface and to clogged pores at the separator side, forming a bottleneck since all ions must pass through it. The usage of porous particles mitigates the effects of binder migration and inhomogeneous binder distribution at high drying rates, explaining the improved rate capability of these electrodes.

This work gives new insights into the differences of electrode structures, which use porous particles instead of the established compact particles. For electrodes with porous particles, it is helpful to know that the beneficial cell performance is solely a consequence of reduced diffusion length and increased contact surface, while the modified pore structure causes increased ionic resistance and limited densification ability, rather representing a shortcoming than providing support to the ion transport conditions.

## Acknowledgments

We acknowledge Zhengqi Wang for preparing and measuring the ionic conductivity of the blocking electrolyte. This work contributes to the research performed at CELEST (Center for Electrochemical Energy Storage Ulm-Karlsruhe) and was funded by the German Research Foundation (DFG) under Project ID 390874152 (POLiS Cluster of Excellence, EXC 2154).

## ORCID

Luca Schneider  <https://orcid.org/0000-0001-6651-7297>  
Werner Bauer  <https://orcid.org/0000-0002-5923-2426>

## References

- D. Deshwal, P. Sangwan, and N. Dahiya, *Wirel. Pers. Commun.*, **124**, 3263 (2022).
- M. Shafiq, M. Rafiq, A. Azam, and X. Luo, *Resour. Conserv. Recycl.*, **178**, 106061 (2022).
- Y. Zhao, O. Pohl, A. I. Bhatt, G. E. Collis, P. J. Mahon, T. R  ther, and A. F. Hollenkamp, *Sustain. Chem.*, **2**, 167 (2021).
- R. Chen, T. Zhao, X. Zhang, L. Li, and F. Wu, *Nanoscale Horizons*, **1**, 423 (2016).
- X. Li, J. Liu, M. N. Banis, A. Lushington, R. Li, M. Cai, and X. Sun, *Energy Environ. Sci.*, **7**, 768 (2014).
- L. S. Kremer, A. Hoffmann, T. Danner, S. Hein, B. Prifling, D. Westhoff, C. Dreer, A. Latz, V. Schmidt, and M. Wohlfahrt-Mehrens, *Energy Technol.*, **8**, 1 (2020).
- J. Landesfeind and H. A. Gasteiger, *J. Electrochem. Soc.*, **166**, A3079 (2019).
- D. Ren, E. Padgett, Y. Yang, L. Shen, Y. Shen, B. D. A. Levin, Y. Yu, F. J. Disalvo, D. A. Muller, and H. D. Abru  a, *ACS Appl. Mater. Interfaces*, **11**, 41178 (2019).
- M. Jiang, Q. Zhang, X. Wu, Z. Chen, D. L. Danilov, R.-A. Eichel, and P. H. L. Notten, *ACS Appl. Energy Mater.*, **3**, 6583 (2020).
- Z. Yang, J. Lu, D. Bian, W. Zhang, X. Yang, J. Xia, G. Chen, H. Gu, and G. Ma, *J. Power Sources*, **272**, 144 (2014).
- B. Lin, Z. Wen, Z. Gu, and S. Huang, *J. Power Sources*, **175**, 564 (2008).
- M. Oljaca, B. Bliznac, A. Du Pasquier, Y. Sun, R. Bontchev, A. Suszko, R. Wall, and K. Koehler, *J. Power Sources*, **248**, 729 (2014).
- A. C. Wagner, N. Bohn, H. Ge  wein, M. Neumann, M. Osenberg, A. Hilger, I. Manke, V. Schmidt, and J. R. Binder, *ACS Appl. Energy Mater.*, **3**, 12565 (2020).
- D. Chen, D. Kramer, and R. M  nig, *Electrochim. Acta*, **259**, 939 (2018).
- M. M  ller, L. Schneider, N. Bohn, J. R. Binder, and W. Bauer, *ACS Appl. Energy Mater.*, **4**, 1993 (2021).
- A. M. Dreizler, N. Bohn, H. Ge  wein, M. M  ller, J. R. Binder, N. Wagner, and K. Andreas Friedrich, *J. Electrochem. Soc.*, **165**, A273 (2018).
- M. Neumann, A. Wagner, N. Bohn, M. Osenberg, A. Hilger, I. Manke, J. R. Binder, and V. Schmidt, *Mater. Charact.*, **155**, 109778 (2019).
- W. Kim, D. Jang, and H. J. Kim, *J. Power Sources*, **510**, 230338 (2021).
- A. C. Wagner, N. Bohn, H. Ge  wein, M. Neumann, M. Osenberg, A. Hilger, I. Manke, V. Schmidt, and J. R. Binder, *ACS Appl. Energy Mater.*, **3**, 12565 (2020).
- J. Klemens, L. Schneider, E. C. Herbst, N. Bohn, M. M  ller, W. Bauer, P. Scharfer, and W. Schabel, *Energy Technol.*, **10**, 2100985 (2022).
- B. Ghanbarian, A. G. Hunt, R. P. Ewing, and M. Sahimi, *Soil Sci. Soc. Am. J.*, **77**, 1461 (2013).
- M. Ben Clennell, *Geol. Soc. Spec. Publ.*, **122**, 299 (1997).
- E. Tsotsas and H. Martin, *Chem. Eng. Process. Process Intensif.*, **22**, 19 (1987).
- P. Zehner and E. U. Schl  nder, *Chemie Ing. Tech.*, **42**, 933 (1970).
- J. Landesfeind, J. Hattendorff, A. Ehrl, W. A. Wall, and H. A. Gasteiger, *J. Electrochem. Soc.*, **163**, A1373 (2016).
- M. Neumann, O. Stenzel, F. Willot, L. Holzer, and V. Schmidt, *Int. J. Solids Struct.*, **184**, 211 (2020).
- D. Sauersteig, N. Hanselmann, A. Arzberger, H. Reinshagen, S. Ivanov, and A. Bund, *J. Power Sources*, **378**, 235 (2018).
- W. Wang, D. Juarez-Robles, and P. P. Mukherjee, *J. Electrochem. Soc.*, **167**, 080510 (2020).
- N. Ogiwara, S. Kawauchi, C. Okuda, Y. Itou, Y. Takeuchi, and Y. Ukyo, *J. Electrochem. Soc.*, **159**, A1034 (2012).
- F. Pouraghajan, A. I. Thompson, E. E. Hunter, B. Mazzeo, J. Christensen, R. Subbaraman, M. Wray, and D. Wheeler, *J. Power Sources*, **492**, 229636 (2021).
- F. Pouraghajan, H. Knight, M. Wray, B. Mazzeo, R. Subbaraman, J. Christensen, and D. Wheeler, *J. Electrochem. Soc.*, **165**, A2644 (2018).
- J. Landesfeind, D. Pritzl, and H. A. Gasteiger, *J. Electrochem. Soc.*, **164**, A1773 (2017).
- D. Pritzl, A. E. Bumberger, M. Wetjen, J. Landesfeind, S. Solchenbach, and H. A. Gasteiger, *J. Electrochem. Soc.*, **166**, A582 (2019).
- M. Gaberscek, J. Moskon, B. Erjavec, R. Dominko, and J. Jamnik, *Electrochim. Solid-State Lett.*, **11**, A170 (2008).
- S. Hein et al., *J. Electrochem. Soc.*, **167**, 013546 (2020).
- A. Shodiev, E. N. Primo, M. Chouchane, T. Lombardo, A. C. Ngandjong, A. Rucci, and A. A. Franco, *J. Power Sources*, **454**, 227871 (2020).
- S. J. Cooper, A. Bertei, D. P. Finegan, and N. P. Brandon, *Electrochim. Acta*, **251**, 681 (2017).
- T. T. Nguyen, A. Demortiere, B. Fleutot, B. Delobel, C. Delacourt, and S. J. Cooper, *NPJ Comput. Mater.*, **6**, 123 (2020).
- S. Malifarge, B. Delobel, and C. Delacourt, *J. Electrochem. Soc.*, **164**, E3329 (2017).

40. M. Kroll, S. L. Karstens, M. Cronau, A. Höltzel, S. Schlabach, N. Nobel, C. Redenbach, B. Roling, and U. Tallarek, *Batter. Supercaps*, **4**, 1363 (2021).
41. J. Landesfeind, M. Ebner, A. Eldiven, V. Wood, and H. A. Gasteiger, *J. Electrochem. Soc.*, **165**, A469 (2018).
42. A. Lasia, *Electrochemical Impedance Spectroscopy and its Applications* (Springer, Boston, MA) p. 1–342 (2014).
43. J. Bisquert, *Phys. Chem. Chem. Phys.*, **2**, 4185 (2000).
44. L. Froboese, P. Titscher, B. Westphal, W. Haselrieder, and A. Kwade, *Mater. Charact.*, **133**, 102 (2017).
45. R. Sim, S. Lee, W. Li, and A. Manthiram, *ACS Appl. Mater. Interfaces*, **13**, 42898 (2021).
46. L. Zielke, T. Hutzenlaub, D. R. Wheeler, I. Manke, T. Arlt, N. Paust, R. Zengerle, and S. Thiele, *Adv. Energy Mater.*, **5**, 1401612 (2014).
47. A. Shodiev, M. Chouchane, M. Gaberseck, O. Arcelus, J. Xu, H. Oularbi, J. Yu, J. Li, M. Morcrette, and A. A. Franco, *Energy Storage Mater.*, **47**, 462 (2022).
48. S. Oswald, D. Pritzl, M. Wetjen, and H. A. Gasteiger, *J. Electrochem. Soc.*, **167**, 100511 (2020).
49. S. Jaiser, J. Kumberg, J. Klaver, J. L. Urai, W. Schabel, J. Schmatz, and P. Scharfer, *J. Power Sources*, **345**, 97 (2017).
50. F. Font, B. Protas, G. Richardson, and J. M. Foster, *J. Power Sources*, **393**, 177 (2018).
51. R. Morasch, J. Landesfeind, B. Suthar, and H. A. Gasteiger, *J. Electrochem. Soc.*, **165**, A3459 (2018).
52. M. Baunach, S. Jaiser, S. Schmelzle, H. Nirschl, P. Scharfer, and W. Schabel, *Dry. Technol.*, **34**, 462 (2016).
53. S. Jaiser, M. Müller, M. Baunach, W. Bauer, P. Scharfer, and W. Schabel, *J. Power Sources*, **318**, 210 (2016).
54. S. Jaiser, N. Sanchez Salach, M. Baunach, P. Scharfer, and W. Schabel, *Dry. Technol.*, **35**, 1807 (2017).